

## RATIR FOLLOWUP OF LIGO/VIRGO GRAVITATIONAL WAVE EVENTS

V. ZACH GOLKHOV<sup>1,2,3,10,11</sup>, NATHANIEL R. BUTLER<sup>3,4</sup>, ROBERT STRAUSBAUGH<sup>4,5</sup>, ELEONORA TROJA<sup>6,8</sup>, ALEXANDER KUTYREV<sup>6</sup>,  
WILLIAM H. LEE<sup>7</sup>, CARLOS G. ROMÁN-ZÚÑIGA<sup>9</sup>, ALAN M. WATSON<sup>7</sup>

*Accepted to AJ*

### ABSTRACT

Recently we have witnessed the first multi-messenger detection of colliding neutron stars through Gravitational Waves (GWs) and Electromagnetic (EM) waves (GW 170817), thanks to the joint efforts of LIGO/Virgo and Space/Ground-based telescopes. In this paper, we report on the RATIR followup observation strategies and show the results for the trigger G194575. This trigger is not of astrophysical interest; however, is of great interest to the robust design of a followup engine to explore large sky error regions. We discuss the development of an image-subtraction pipeline for the 6-color, optical/NIR imaging camera RATIR. Considering a two band (*i* and *r*) campaign in the Fall of 2015, we find that the requirement of simultaneous detection in both bands leads to a factor  $\sim 10$  reduction in false alarm rate, which can be further reduced using additional bands. We also show that the performance of our proposed algorithm is robust to fluctuating observing conditions, maintaining a low false alarm rate with a modest decrease in system efficiency that can be overcome utilizing repeat visits. Expanding our pipeline to search for either optical or NIR detections (3 or more bands), considering separately the optical *riZ* and NIR *YJH* bands, should result in a false alarm rate  $\approx 1\%$  and an efficiency  $\approx 90\%$ . RATIR's simultaneous optical/NIR observations are expected to yield about one candidate transient in the vast  $100 \text{ deg}^2$  LIGO error region for prioritized followup with larger aperture telescopes.

*Subject headings:* gravitational waves — galaxies: statistics — methods: observational — catalogs

### 1. INTRODUCTION

The first ever direct detection of the GW signal, GW150914, was made by advanced-LIGO (Aasi et al. 2015) in September 2015 (Abbott et al. 2016a) from a binary BH merger (Abbott et al. 2016b). This discovery entered us into the GW era; however, complementary identification of EM counterparts to GW events is required to guide us to the next stage: the GW-EM multi-messenger astronomy era (Bloom et al. 2009a; Nissanke et al. 2010; Metzger & Berger 2012; Branchesi 2016).

A joint EM-GW detection would constrain some fundamental physical properties of compact binary coalescence (CBC) events such as the distance scale, luminosity, and host galaxy environment. However, identifying a counterpart is remarkably challenging due to the LIGO inherently weak localization of GW events ( $\sim$  a few hundred  $\text{deg}^2$ ). Nonetheless, the scientific returns of such discovery justify many efforts taken, even a small step forward.

CBC events represent powerful engines for the production of gravitational (see, e.g., Thorne 1987; Phinney 1991; Bel-

czynski et al. 2002; Abadie et al. 2010), EM, and neutrino radiation (e.g., Ando et al. 2013). In the CBC model, a neutron star (NS) and compact companion in an otherwise stable orbit lose energy to gravitational waves (e.g., Thorne 1987; Nakar 2007; Lee & Ramirez-Ruiz 2007). Disruption of the NS(s) is thought to produce an accretion disk, which may power relativistic outflows of variable Lorentz factor (Rezzolla et al. 2011; Ruiz et al. 2016). Internal shocks in the relativistic jets are expected to produce brief, strong, collimated gamma-ray emission and external shocks with the circumstellar material are expected to produce the lower-energy emission on longer timescales (e.g., Rees & Meszaros 1992; Piran 1999). Short-duration Gamma-ray Bursts (sGRBs; Kouveliotou et al. 1993) provide our best potential link to gravitational wave sources. If these events are due to collapse-object mergers (e.g., Nakar 2007; Lee & Ramirez-Ruiz 2007), copious gravitational waves are expected, and these can be detected by Advanced LIGO if the source is sufficiently nearby. Indeed, due to beaming (Burrows et al. 2006; Troja et al. 2016b), the LIGO rate should be significantly larger (factor 10; Chen & Holz 2013) than the observed sGRB rate.

Finding the potentially rapidly fading afterglow of a GW source requires the engagement of facilities world wide with fast response times. Many facilities have participated in the search for the EM counterparts of LIGO GW events – in the optical, X-ray, and radio bands – and have reported their followup strategies to the community (e.g., Connaughton et al. 2016; Evans et al. 2016; Kasliwal et al. 2016; Smartt et al. 2016; Soares-Santos et al. 2016; Díaz et al. 2016; Troja et al. 2016a). We do not expect to see EM emission from BH-BH mergers, so we are mainly focused on mergers involving at least one NS.

Here, we present the Reionization and Transients InfraRed (RATIR) observatory followup effort. RATIR is a simultaneous 6-filter imaging camera (*r* band through *H* band), mounted on a Harold L. Johnson 1.5-meter telescope at Ob-

<sup>1</sup> DiRAC Institute, Department of Astronomy, University of Washington, 3910 15th Avenue NE, Seattle, WA, 98195, USA

<sup>2</sup> The eScience Institute, University of Washington, Seattle, WA 98195, USA

<sup>3</sup> School of Earth and Space Exploration, Arizona State University, Tempe, AZ 85287, USA

<sup>4</sup> Cosmology Initiative, Arizona State University, Tempe, AZ 85287, USA

<sup>5</sup> Physics Department, Arizona State University, Tempe, AZ 85287, USA

<sup>6</sup> NASA, Goddard Space Flight Center, Greenbelt, MD 20771, USA

<sup>7</sup> Instituto de Astronomía, Universidad Nacional Autónoma de México, Apartado Postal 70-264, 04510 México, D. F., México

<sup>8</sup> Department of Astronomy, University of Maryland, College Park, MD 20742, USA

<sup>9</sup> Instituto de Astronomía, Universidad Nacional Autónoma de México, Unidad Académica en Ensenada, Ensenada BC 22860, México

<sup>10</sup> Moore-Sloan Fellow

<sup>11</sup> Dirac Fellow

servatorio Astronómico Nacional on Sierra San Pedro Mártir, Baja, CA, MX (Butler et al. 2012; Watson et al. 2012). The NIR capability of RATIR is highly desirable, with the recent suggestion that some sGRBs may be associated with very red “kilonova” events (Barnes & Kasen 2013; Tanvir et al. 2013, see also Jin et al. 2015, 2016). As an approximately isotropic EM counterpart to the GW signal (Bloom et al. 2009b; Roberts et al. 2011; Metzger & Berger 2012; Piran et al. 2013; Metzger 2017), kilonovae provide a unique and direct probe of an important  $r$ -process site (e.g., Rosswog et al. 2014). A kilonova within 100 Mpc would likely be quite bright in the NIR and amenable to detection. At such distances the source in Tanvir et al. (2013) would have  $H < 18.5$  mag (AB). RATIR reaches  $10\sigma$  limiting AB magnitudes in 10 minutes of 22.0, 21.4, 20.2, 19.7, 19.6, 18.9 in the *riZYJH* bands, respectively.

In this paper, we focus our analyses on the trigger G194575 (Singer et al., GCN 18442), which we were able to promptly observe in Fall 2015 (Butler et al., GCN 18455). Despite the fact that this trigger was later found to be unrelated to any astrophysical object later (LIGO Scientific Collaboration, GCN 18626), the rather larger error region  $\sim 1000$  deg<sup>2</sup> provided us a highly challenging exercise for the design of a robust exploratory pipeline. Similar to other triggers received from the LIGO collaboration team, the EM counterpart followup community responded quickly to the trigger and was actively engaged until its non-astrophysical origin became apparent. During that time, ground-based observatories reported two sources of potential interest regarding the trigger, LSQ15bjb detected by the La Silla-QUEST (Rabinowitz et al., GCN 18473) and iPTF15dld detected by the iPTF (Singer et al., GCN 18497). RATIR observed the La Silla - QUEST candidate and reported a clear detection of the source in the *i*, *r*, and *z* bands (Golkhou et al., GCN 18500).

In section 2, we describe the survey strategy, data reduction, and analysis of the designed EM counterparts discovery pipeline. Field targeting and scheduling along with identification and rejection of bad subtractions are presented in section 3. In section 4, we discuss our results, the expected false alarm and success rate, and address the community benefits from the RATIR pipeline. All magnitudes in the paper are in the AB system.

## 2. SURVEY STRATEGY, DATA REDUCTION, AND ANALYSIS

A search over the entire LIGO detector error region (several hundred square degree) using a narrow field of view (five to ten arcminute) instrument like RATIR is unfeasible due to observing time constraints. It is simply not possible to complete the survey sufficiently rapidly (within a few days) in two or more epochs to allow for a comprehensive search for variable, new objects. Instead, we target only portions of the LIGO error regions most likely to contain sGRBs.

In our strategy (Section 2.1), we search a much smaller portion of the LIGO error region by crossmatching GW galaxy catalog (White et al. 2011) sources and including only very bright luminous galaxies (Gehrels et al. 2016). The candidate galaxies selected based on a population-half-light criteria using the absolute *B*-band magnitudes, and are scheduled for visits twice per field. Return visits for image subtraction purposes are conducted on a subsequent nights.

With two or more frames captured for each target galaxy field, we performed digital image subtraction with the High Order Transform of PSF AND Template Subtraction (HOTPANTS; Becker 2015). HOTPANTS is an implementation of

the Alard & Lupton (1998) algorithm, based on a spatially-variable kernel method that matches the PSFs of two astronomical images. Prior to running, the images are bias, dark, and sky-subtracted, flat-fielded, and astrometrically co-aligned using SWARP (Bertin et al. 2002). We use the Source Extractor (Bertin & Arnouts 1996) software to identify sources for alignment and to estimate the image FWHM values. The quadrature difference between FWHM values is used to define the starting Gaussian sigma values for the HOTPANTS convolution. Custom point-spread-function (PSF) fitting software is used to estimate the image PSF and to obtain photometry for the difference frames. In our final photometric detections, we require  $\geq 10\sigma$  detections.

While our image subtractions are typically very clean (e.g., Figure 2), residual flux can often be detected near bright sources or new image boundaries. These false sources are flagged and ignored (see Figure 3) by identifying a bright cataloged source within 10 arcsec, by comparing the (typically small) FWHM of the source relative to the median FWHM of the image, or by discarding sources near the image boundaries. Bad subtractions can also be obtained, typically yielding a large number ( $> 10$ ) of detections. We have developed an automated filtering approach to minimize these cases using image quality metrics present prior to subtraction (Section 3.1).

We distinguish among three types of false alarms: non-astrophysical fake signals (largely from bad subtractions); known asteroids and other known solar system bodies; and astrophysical transients that do not correspond to the GW events. In this work, we focus on filtering out the first type.

### 2.1. Galaxy Strategy

A typical LIGO sky map error region is much larger than the field of view of optical or X-ray telescopes. Due to the time constraints of rapid followup, covering a few hundred or even a few tens of the sky square degrees is not a practical approach by a small FoV telescope. Therefore, finding an optimal strategy which determines the ideal domain of investigations should be at the core of any pipeline designs of LIGO GW followup sources (e.g., Hanna et al. 2014; Bartos et al. 2015). A catalog of galaxies which has already satisfied some critical criteria relevant to our search is required. These criteria are adequate sky coverage, sufficient depth, and galaxy brightness (high blue luminosity). The latter condition is important because blue luminosity is a tracer of recent star formation and sources produced by stars ought to track the light.

The Gravitational Wave Galaxy Catalog (GWGC; White et al. 2011) is an attempt to offer such a galaxy catalog and has been used by many followup groups e.g. DLT40, Swift-XRT, UL50, Kanata, OAO-WFC, and RATIR. We used GWGC as our main catalog during *O1* while also following a similar galaxy strategy as Gehrels et al. (2016) which considers only brighter galaxies that produce  $\sim 50\%$  of the light. This constrains the absolute blue magnitude of galaxies to less than  $-20.025$  mag; eliminating  $\sim 80\%$  of galaxies in the GWGC.

The modified GWGC is complete  $\sim 100\%$  out to about 60 Mpc which is consistent with the LIGO estimate of sensitivity coverage during *O1* run. The estimate of completeness is defined based on *B*-band magnitude which is expected to follow sGRB rate (Fong et al. 2013). At distances  $\sim 100$  Mpc, the GWGC completeness reduces to about 85% for the selected bright galaxies (see the figure 3 of Gehrels et al. 2016). Caution will be necessary during the LIGO *O2* and later runs

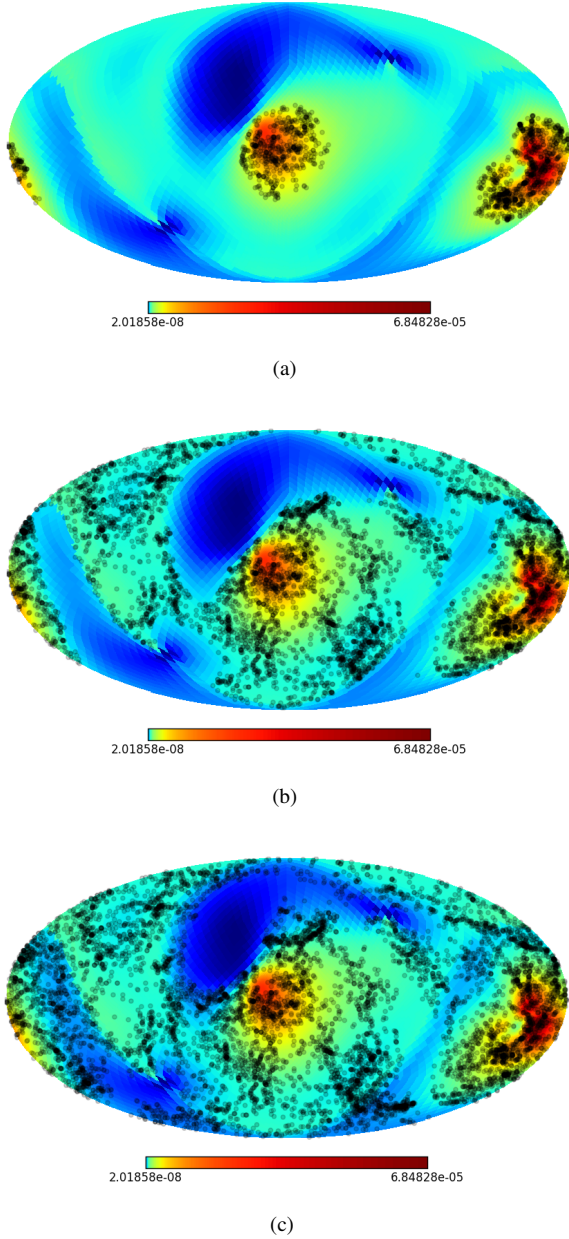


FIG. 1.— The BAYESTAR GW probability skymap in  $\log$  for trigger G194575 over-plotted with the list of galaxies in the GWGC with black dots for  $1\sigma$  (fig. 1a),  $2\sigma$  (fig. 1b), and  $3\sigma$  (fig. 1c).

since we expect to detect GW events due to the binary NS at distances exceeding 100 Mpc (Abbott et al. 2016c), beyond which the incompleteness of the GWGC increases. New catalogs more suitable for the next LIGO runs are under construction (e.g. CLU, Gehrels et al. 2016, and GLADE<sup>12</sup>, Dalya et al. 2016).

### 3. FIELD TARGETING AND SCHEDULING

Upon a trigger, our pipeline automatically receives the probability skymap error region from the LIGO collaboration. The sky localization is provided at low-latency by the “BAYESTAR” and “CWB” pipelines, and later with “LALInference”. The skymap error region is projected onto the modified GWGC, as described in the previous section, and a list of

candidate galaxies is made. Figure 1 shows the BAYESTAR GW probability skymap for trigger G194575 (Singer et al., GCN 18442). Regions with the darker red color represent higher probability GW source localization and regions with the darker blue color are associated with the lowest probability GW source locations. The color bar shows the corresponding probability values. The GWGC contains 53,312 galaxies and our bright galaxy criterion ( $x_{1/2} > 0.626$ , see Gehrels et al. (2016) for details) typically passes only  $\sim 20\%$  in a given sky area. Projecting the G19475 skymap within  $1\sigma$  error region onto our galaxy catalog results in 1539 candidate galaxies which are shown with black circles in Figure 1a. This number increases to 6057 and 8217 for  $2\sigma$  (fig. 1b) and  $3\sigma$  (fig. 1c), respectively.

Given that not all of these galaxies will be visible at OAN-SPM, we expect to followup about half of the galaxies in the list. This is still a large number even for the  $1\sigma$  error region. The RATIR scheduler selects and queues targets automatically to be imaged at the first available time. Nominally, we also rank the list of candidate galaxies based on the  $B$ -band luminosity value. It is also possible to prioritize based on distance estimates provided in the LIGO/Virgo GCN notices. However, an estimate of the LIGO GW source distance was not available during the *O1* run.

Given the available observing time, we observed 26 nearby galaxies ( $D < 10$  Mpc) within the GWGC catalog and contained within the  $1\sigma$  LIGO/Virgo error region for trigger G194575 (Singer et al., GCN 18442). Between RA 23.1 hours and RA 1.5 hours (J2000) with RATIR on the night of 2015/10/23, we obtained a total exposure of  $\sim 8$  minutes on each of the 26 fields (see Table 1), reaching typical depths of  $r$  and  $i = 21$  mag (AB,  $10\sigma$ ). These magnitudes are not corrected for Galactic extinction. Each field, centered upon one GWGC galaxy, has a size of approximately  $5 \times 5$  arcmin<sup>2</sup>. We observed these fields on two more consecutive nights (10/24 and 10/25; Table 1). We had a typical image quality of 1.8 arcsec each night. To reach comparable limiting magnitudes on the third and final night, a 50% increase in exposure time was required to overcome highly non-photometric observing conditions. On the first two nights, the  $i$ -band zero points were stable (to within 10%) while the zero point varied by nearly a factor of unity on the third night. The NIR RATIR channels (ZYJH) were not available at this time.

Figure 2 shows a gallery of image subtraction frames for targets #14, #16, and #23 in the  $i$  and  $r$  bands. The images on the left, middle, and right columns show science, reference, and the subtracted frames, respectively. We note that the image subtraction is typically extremely clean. Each of the selected targets shown in the Figure 2 represents a different type of target field. Target #14 is a very crowded field with many stars in the foreground and thus not very deep. Target #16 is a deep image with the targeted galaxy in the center and adequate sources for the alignment task, ideal for our purpose. Target #23 is a semi-crowded field with manageable number of sources for image-subtraction. Detected sources are marked with red squares in the science and subtracted frames. Fields #14 and #16 contain only one false detection in the  $i$  band. In field #23, each of the  $i$  and  $r$  bands comprises two false detections; however, only one of them appears in the same position on the two frames.

Observations obtained on the first night are compared with SDSS images, if available, as reference frames to detect any potential targets. The RATIR pipeline starts observing the LIGO/Virgo error region immediately after receiving a trig-

<sup>12</sup> <http://aquarius.elte.hu/glade/>



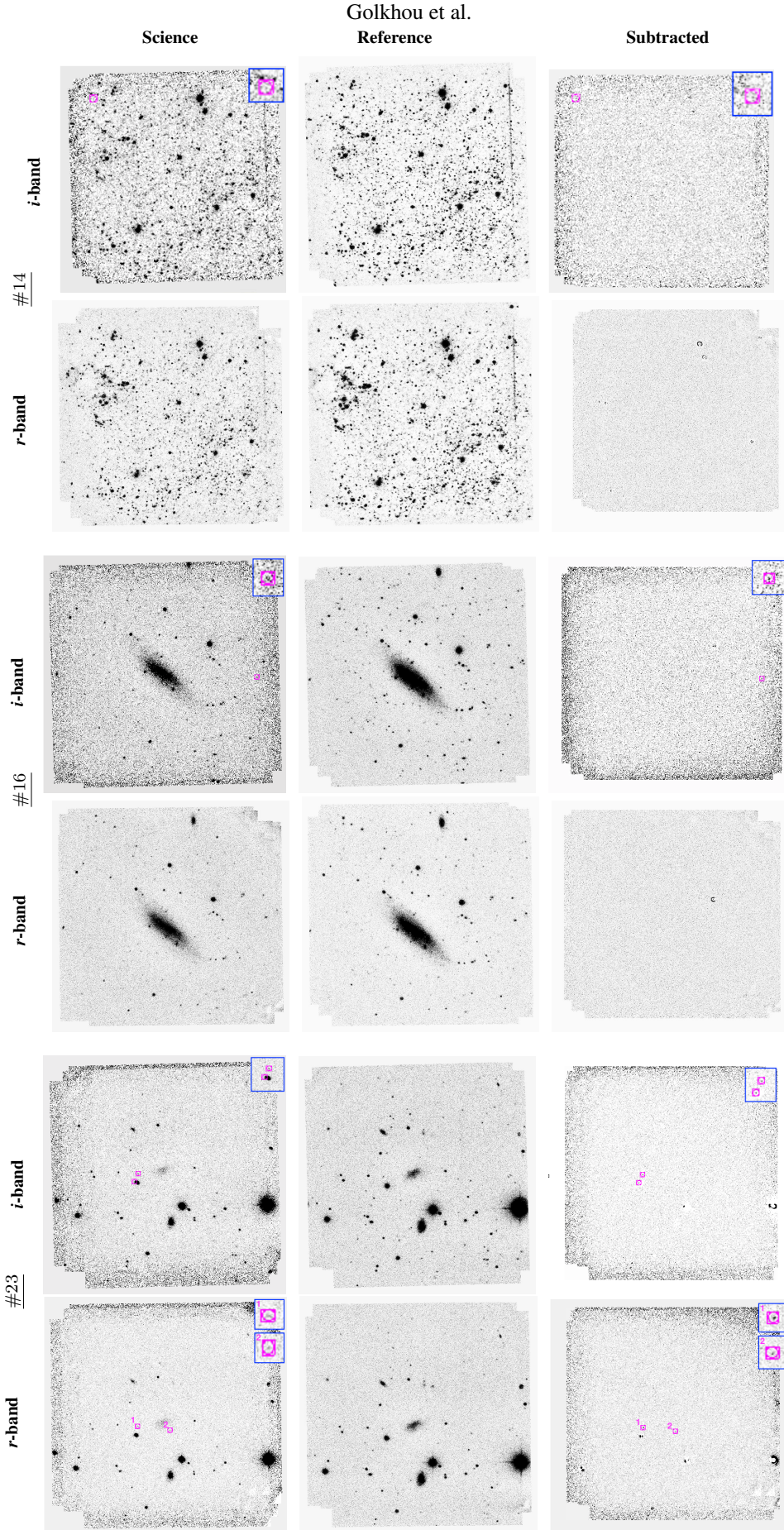


FIG. 2.— A gallery of image subtraction frames for targets #14 (1<sup>st</sup> & 2<sup>nd</sup> rows), #16 (3<sup>rd</sup> & 4<sup>th</sup> rows), and #23 (5<sup>th</sup> & 6<sup>th</sup> rows) in the *i* and *r* bands. The images on the left, middle, and right show science (10/24), reference (10/23), and the subtracted frames, respectively. Detected sources marked with red squares in the science and subtracted frames. The sizes of all the postage-stamps are:  $5 \times 5 \text{ arcmin}^2$ .



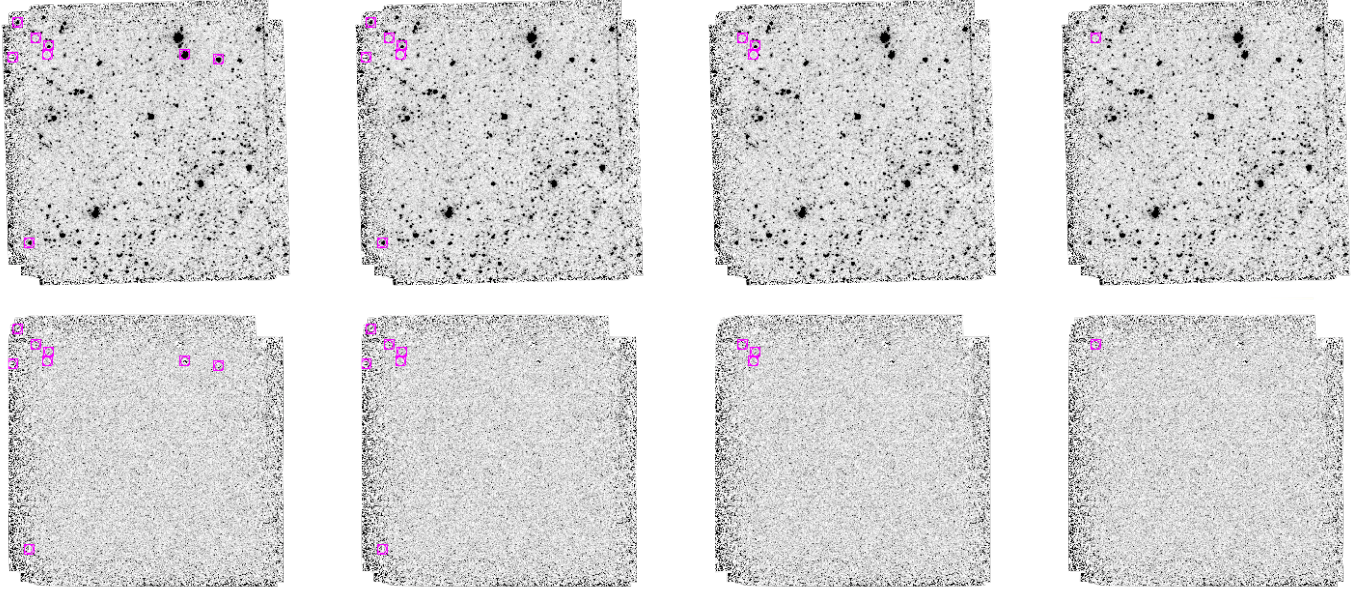


FIG. 3.— Various steps of removing false detected sources marked with red squares of target #14 in the source frame  $i$ -band (top row) and the subtracted frame (bottom row). All the raw detected sources are shown in the first column (no filter). The initial step of filtering rejects multiple detections around same stars (second column). The subsequent step of filtering removes false detections on the edge of a frame ( $\text{'distance to edge'} < 62$  pixel). The last step of filtering rejects extra clustered detections around a source ( $\text{'cluster radius'} < 14$  arcsec). The sizes of all the postage-stamps are:  $5 \times 5$  arcmin<sup>2</sup>.

ger form the LIGO team. Any meaningful changes in the magnitude of a true candidate source should evolve during the consecutive nights in which we are able to detect. Given the requirement of  $10\sigma$  threshold detection in our designed pipeline, any changes of magnitude  $\gtrsim 0.1$  mag should be detected.

### 3.1. Identifying and Ignoring Bad Subtractions

We now implement our modified image-subtraction routine (Section 2) to detect any possible transients (as an example, see Figure 3). The top row in Figure 3 shows target #13 (science frame from 10/24) and the bottom row shows the subtracted frame (the 10/23 frame was used as the reference frame). Each column shows various steps of removing false detections. No filter is implemented for the first column. The initial step of filtering rejects multiple detections around same stars (second column). The subsequent step of filtering removes false detections on the edge of a frame ( $\text{'distance to edge'} < 62$  pixel). The last step of filtering rejects extra clustered detections around a source ( $\text{'cluster radius'} < 14$  arcsec). The implemented actions, the presented hierarchical steps, and the numbers described here are the outcome of a comprehensive statistical analysis with the objective of reducing image subtraction residuals.

In principle, having observed 26 galaxy targets in 2 optical bands for 3 consecutive nights, we can carry-out  $26 \times 3 \times (2) \times 2 = 312$  different image subtractions. The extra factor of 2 takes into account the two possible way of subtracting two images. In practice, we would like to only conduct one subtraction per field in a way that yields the highest quality subtraction. We now use all possible subtractions to explore how to find the best possible subtraction.

Figure 4 shows a histogram of the number of detections in all frames. The number of false detections is zero for about half of the frames. For 90% of the rest is less than 10 detections, and we take  $< 10$  detections to define a good sub-

traction. A well-posed subtraction will always have a deeper reference frame with better seeing as compared to the science frame. However, because our (time-limited) observation strategy typically leads to similar depths for both *science* and *reference* frames, it is often not possible (e.g. due to changing sky transmission) to know a-priori how to do the subtraction. Nevertheless, image statistics determined pre-subtraction can help us to address this problem.

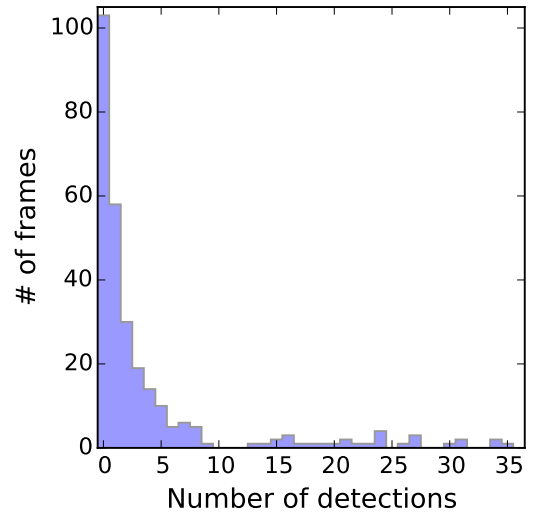


FIG. 4.— Histogram of number of detections in all frames.

We exploit the following image-quality statistics and seek to understand how these can be used to avoid bad subtractions: (1) the ratio of the PSF sigma in the science frame over the PSF sigma in the template, (2) the ratio of number of stars in science and template frames, and (3) the median of the RMS-

fraction between science and template frames. Hereafter, we refer to these parameters as  $Par_1$ ,  $Par_2$ , and  $Par_3$ , respectively. We now seek to define a sequential filtering on these parameters – to be coded into an image subtraction wrapper – that yields the most compact  $K\%$ -Confidence Interval (C.I.; Eq. 1), e.g. 90%, dumping outliers).

$$\text{C.I.} = P(a_k \leq Par_k \leq b_k) \quad (1)$$

Here subscript  $k = [1, 2, 3]$  and the  $a$  and  $b$  values specify the parameter lower and upper bounds that contain C.I. percent of that parameter space.

Figure 5 shows scatter plots of the  $Par_1$ ,  $Par_2$ , and  $Par_3$  values of all subtracted images versus their number of detected sources, separately. It also presents the three stages of filtering implementing consecutively on their parameter spaces, in the same order. The  $Par_1$  data within  $[a_1, b_1]$  range feeds to the second filter which implements on the  $Par_2$  space, and so forth, the  $Par_2$  data within  $[a_2, b_2]$  range feeds to the third filter which implements on the  $Par_3$  space. To reach the 90%-C.I. at the end of filtering task, the image subtraction wrapper figures out how to set the same value of  $K$  between the filtering stages. Cuts in the parameter space are shown with dashed lines in the Figure 5.

The expected performance of the image subtraction wrapper as the C.I. is varied can be visualized (Figure 6) by plotting the *Bad* subtraction rate versus image retention rate. We define in Equation 2 the image retention rate,  $r_{\text{rtn}}$ , of a filter as the ratio of number of accepted *Good* subtracted frames,  $G_i$ , over the total number of input frames. Similarly, the *Bad* subtraction rate,  $r_{\text{sb}}$ , is defined as the ratio of the number of accepted *Bad* frames,  $B_i$ , over the total number accepted frames,  $B_i + G_i$  (Eq. 3). Subscripts  $i$  and  $o$  represent data inside and outside of the  $[a_k, b_k]$  interval, respectively.

$$i \in [a_k, b_k] \quad o \notin [a_k, b_k]$$

$$\text{Image retention rate : } r_{\text{rtn}} = \left( \frac{G_i}{\sum \text{frames}} \right) \quad (2)$$

$$\text{Bad subtraction rate : } r_{\text{sb}} = \left( \frac{B_i}{B_i + G_i} \right) \quad (3)$$

Blue squares in Figure 6 represent the data points based on the  $i$ -band data as the test set and red circles show the data points based on the  $r$ -band data as the test set. Black diamonds correspond to use of both  $r$  and  $i$  bands. The tight clustering of these three curves in Figure 6 illustrates that the filtering system is quite robust with respect to which data are used to train and test and can achieve high image retention rates ( $\sim 90\%$ ) with low bad subtraction rates ( $\sim 4\%$ ). For comparison purposes, the efficiency of the system prior to the filtering process, raw data, is also displayed on the Figure 6 with a yellow star. We adopt the circled black diamond in Figure 6 as our final bad subtraction filter. To reach this performance, the wrapper sets the following constraints for each of the  $Par_1$ ,  $Par_2$ , and  $Par_3$  values as  $[0.64, 1.45]$ ,  $[0.53, 2.5]$ , and  $[0.55, 2.17]$ , respectively.

For each of the imaged fields on two different epochs in our data set, we may now identify the optimal subtraction approach prior to performing the subtraction. This procedure is described using a *flowchart* presented in the Figure 7. The detailed steps in the *flowchart* are performed for each of the imaged fields in the  $i$  and  $r$  bands, separately. We note that,

as the last step, a visual inspection is conducted to remove frames with spurious features like satellite trails.

#### 4. RESULTS & DISCUSSION

RATIR performed rapid-response followup to the second GW trigger released to the EM partners by the LIGO team during the *O1* operating run. The observing time constraints allowed us to image 26 galaxies ( $D < 10$  Mpc; Table 1). The candidate fields were followed for two more consecutive nights. We imaged each of the 26 fields in both the  $i$  and  $r$  bands and performed our modified image subtraction routine to search for any possible transients.

For the 25 imaged fields on 10/23 and 10/24 nights, we found only two fields (out of 20) yielded more than zero detections at the same sky position in the both  $i$  and  $r$  bands. From this, we can estimate a false-alarm-rate (FAR) of  $2/20 = 0.1$  and an efficiency of  $20/25 = 0.8$ . This is an “AND” rule for comparing the  $r$  and  $i$  bands to find detections. We can also consider an “OR” rule, either  $i$  or  $r$  band detections. We find FAR and efficiency values of 0.64 and 0.92, respectively, in this case. These results and those including the 10/25 night are shown in the Figure 8. The advantage of multi-bands imaging is clear.

Inspections of all the imaged fields on 10/25 epoch demonstrate a higher level of background noise – compared to the two previous epochs – due to the non-photometric conditions. This effect impacts primarily the detection efficiency as shown in the Figure 8.

Since the G19475 trigger was not of astrophysical origin, we did not expect to ascertain a real transient associated with the event. Therefore, we are not able to determine a true sensitivity. To validate the sensitivity of our approach, we analyze a set of supernova images captured with RATIR (PI, Ori Fox). The SNe images were taken using both RATIR’s optical and Infra-red bands. Studying 5 SNe fields in the *irZYJH* bands for two different epochs, we verified that all difference frames containing a  $10\sigma$  flux excess are indeed recovered via our methodology.

Similar to Kessler et al. (2015), we find the image subtractions efficiency in our proposed pipeline would not degrade with increasing galaxy surface brightness at the lower redshifts ( $z < 0.5$ ), which is the case in our search. Therefore, the bright-galaxy issue has minimal impact on our discovery program here.

##### 4.1. End-to-End Sensitivity and False Alarm Rate

Given RATIR’s simultaneous optical/NIR observing capability, an optimal strategy – which reduces *FAR* as much as possible while keeping sensitivity high – would be searching for either optical or NIR detections (3 or more bands), considering separately *riZ* and *YJH*. This can be viewed as a sGRB strategy with optimal depth (using the *riZ* filters), combined with a simultaneous NIR (*YJH* band) survey to find potential kilonovae. Extrapolating our results from optical bands ( $i$  and  $r$ ), we expect a 3-band survey to exhibit a  $FAR \approx 1\%$  and an image-retention efficiency  $\approx 90\%$ , provided that multiple nights are allocated to re-observe targets missed initially. We note that a simultaneous multicolor approach is typically employed to increase the probability of detection (see e.g. Szalay et al. 1999); however, our approach is somewhat different in that we utilize the multiple bands to maintain ( $10\sigma$ ) detection capability while greatly minimizing false alarms. This is a crucial aspect of the RATIR followup engine as it will add the most confidence to justify additional observing requests with

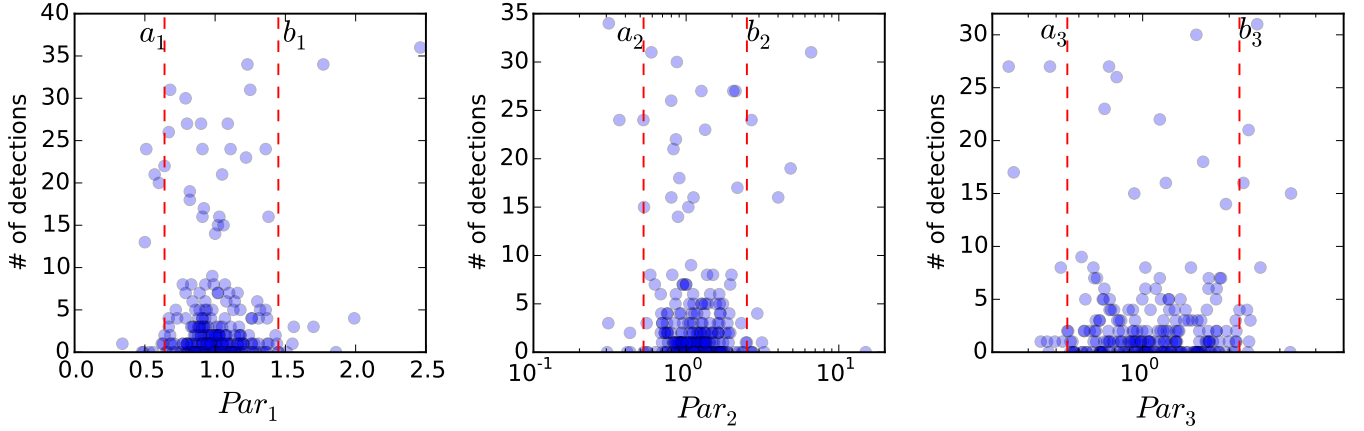


FIG. 5.— Three stages of filtering implementing consecutively on the  $Par_1$  ( $\sigma_{\text{sci}}/\sigma_{\text{tmp}}$ ),  $Par_2$  ( $N_{\text{sci}}^*/N_{\text{tmp}}^*$ ), and  $Par_3$  ( $RMS_{\text{sci}}/RMS_{\text{tmp}}$ ) parameter spaces, in order. Cuts in the parameter space keep data within the most compact 90%-confidence interval and are shown with dashed lines.

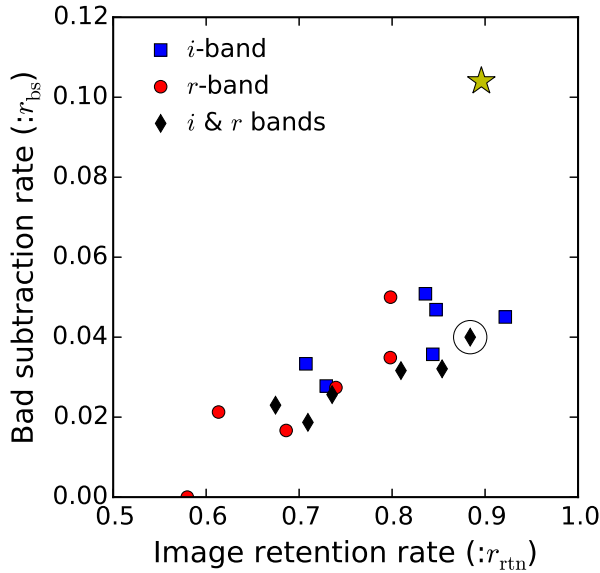


FIG. 6.— Yellow star: the performance of the system before filtering process (raw data). Blue squares: the wrapper performance estimations based on the  $i$ -band data as test set, while the  $r$ -band data was used as the training set (a 2-fold cross validation). Red circles: the wrapper performance estimations estimated based on the  $r$ -band data as test set, while the  $i$ -band data was used as the training set. Black diamonds: the wrapper performance estimations estimated based on both  $i$  and  $r$  bands. The circled black diamond specifies our desired system efficiency. *The wrapper delivers a robust performance independent of the input.*

larger aperture facilities. We have rigorously tested the trade-off between false alarm rate and sensitivity in the design of our implemented methodology.

In order to estimate the total system throughput for potential EM gravitational wave counterparts detected by RATIR, we adopt a similar LIGO (and Virgo) error region fraction value as Gehrels et al. (2016) for  $O2$  (2017)  $\sim 100 \text{ deg}^2$ . If we utilize the GWGC nearby galaxy catalog and select the brightest galaxies representing half of the population light (1 galaxy per  $\text{deg}^2$ , White et al. 2011), we can concentrate observations on about 100 galaxies in the LIGO (and Virgo)  $3\sigma$  error region. Given that not all the candidate galaxies in our list will be vis-

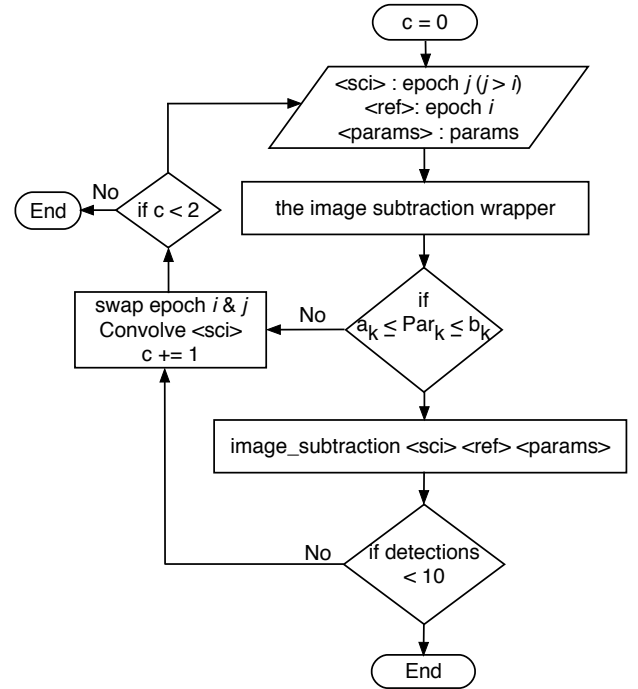


FIG. 7.— *Flowchart.* The procedure to determine how best to subtract two images to yield a reliable result (detections < 10).

ible at the RATIR observatory site, we expect the candidates list to be reduced by about half. As mentioned in the Section 1, RATIR reaches its design  $10\sigma$  limiting magnitude in about 10 minutes, and the candidate sources are expected to be brighter than our limiting magnitudes. Allowing for a conservative overhead of 20% for slew between galaxy positions, we expect to be able to survey all the galaxies in about 10 hrs. In this case of narrower regions, we are able to integrate more deeply and also to check for same variability same night. Our nominal strategy is then to re-observe the field the next night (or the night after in the case of poor weather) to check for variability.

The brighter galaxy selection of the GWGC maintains a galaxy completeness near 100% to a distance of  $\sim 90 \text{ Mpc}$  and drops to 85% at the distance of  $\sim 100 \text{ Mpc}$  as the upper bound region. The error region source fraction resulting from the wrapped image subtraction approach reduces the search



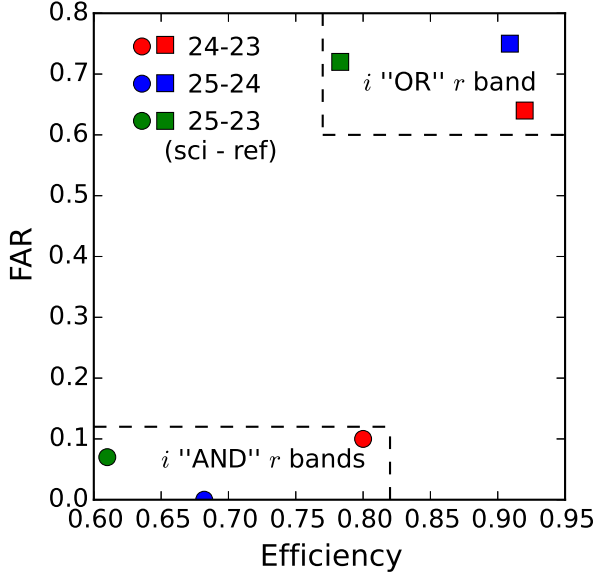


FIG. 8.— FAR and efficiency of the designed EM counterparts to GW events pipeline. Candidate galaxies are imaged on three subsequent epochs, 2015/10/23, 10/24, and 10/25. Algorithm throughput represents with circles if we require both  $i$  “AND”  $r$  bands and with squares if we require either  $i$  “OR”  $r$  band. The combination of multiple frames drives the FAR down as  $\lesssim 0.1^{N_f-1}$  ( $N_f$  depicts the number of available filters).

space region to about 90% as the image retention rate. Our automated pipeline flags  $\sim 1\%$  of the candidate imaged fields as potential targets for the additional followup. Combining the galaxy completeness ( $\approx 50\%$ ) with the RATIR survey completeness ( $\approx 45\%$ ), limited primarily by observability, we estimate a final success rate of  $\approx 20\%$ . This is an excitingly large number, given the great scientific impact of an identified EM counterpart to a gravitational wave event. The possibility of multiple followup campaigns of separate triggers only increases our chances. In 2016/2017 RATIR observed additional LIGO fields, and analysis is underway.

As LIGO/Virgo sensitivity increases, we will require a galaxy catalog which covers distances up to  $\sim 450$  Mpc (Bartos et al. 2013) with greater completeness than is currently available. There are some attempts to combine other galaxy catalogs e.g., the 2MASS Photometric Redshift Catalog (2MPZ; Bilicki et al. 2014) with the GWGC, as a short-term plan (see also Gehrels et al. 2016; Dalya et al. 2016) and also efforts to constrain the exact GW distance scale (Singer et al. 2016). We plan to adopt a more complete galaxy catalog in our pipeline as it becomes available. We have been actively following LIGO triggers during the O2 run as well as candidate counterparts reported by other EM followup groups.

The results of our observations reported in LVC/GCN circulars (e.g., Golkhou et al., GCN 20485).

Combining a distance and position information from the GW observations provided during LIGO/Virgo O2 run with our compiled list of nearby galaxies can reduce the search space and help to prioritize targets for further followup. Since we are more interested in the impact of the galaxy catalog we follow a similar strategy as Gehrels et al. (2016) and assume that the localization subtends a given solid angle, which is a shell between two constant radii. Having a target distance information such as a BBH event at a distance of 350 Mpc with an uncertainty of 25-30% (see for example, Cutler & Flanagan 1994; Berry et al. 2015) would reduce the volume, and hence number of galaxies, by a factor of 50-60%. This is in agreement with the finding of Nissanke et al. (2013).

RATIR multicolor observations can provide powerful discriminating information for candidates found by other facilities. In the case of immediate, robotically-triggered observations following a LIGO detection, RATIR’s narrow field of view ( $\lesssim 10$  arcmin) dictates a search strategy which targets nearby galaxies within the large LIGO error circles. These nearby events are, in turn, the most likely to yield decisive CBC associations. As a 6-filter, multicolor instrument, RATIR’s simultaneous observations of candidates greatly reduces the number of false alarms, while also providing spectral information and additional time-sampling (see e.g., Golkhou & Butler 2014; Littlejohns et al. 2014; Golkhou et al. 2015c), important for afterglow studies. Moreover, with the recent clue that some sGRBs may be associated with very red “kilonova” events (Barnes & Kasen 2013; Tanvir et al. 2013, see also Jin et al. 2016), NIR observations may be essential to afterglow detection.

We thank the RATIR project team and the staff of the Observatorio Astronómico Nacional on Sierra San Pedro Mártir, and acknowledge the contribution of Leonid Georgiev to its development. RATIR is a collaboration between the University of California, the Universidad Nacional Autónoma de México, NASA Goddard Space Flight Center, and Arizona State University, benefiting from the loan of an H2RG detector and hardware and software support from Teledyne Scientific and Imaging. RATIR, the automation of the Harold L. Johnson Telescope of the Observatorio Astronómico Nacional on Sierra San Pedro Mártir, and the operation of both are funded through NASA grants NNX09AH71G, NNX09AT02G, NNX10AI27G, and NNX12AE66G, CONACyT grants INFR-2009-01-122785 and CB-2008-101958, UNAM PAPIIT grant IN100317, and UC MEXUS-CONACyT grant CN 09-283. We also thank our referee for insightful comments that improved the manuscript.

## REFERENCES

- Aasi, J., Abadie, J., Abbott, B. P., et al. 2015, *Classical and Quantum Gravity*, 32, 115012
- Abadie, J., Abbott, B. P., Abbott, R., et al. 2010, *Classical and Quantum Gravity*, 27, 173001
- Abbott, B. P., Abbott, R., Abbott, T. D., et al. 2016a, *Physical Review Letters*, 116, 131103
- . 2016b, *Physical Review Letters*, 116, 241102
- . 2016c, *Living Reviews in Relativity*, 19, 1
- Alard, C., & Lupton, R. H. 1998, *ApJ*, 503, 325
- Ando, S., Baret, B., Bartos, I., et al. 2013, *Rev. Mod. Phys.*, 85, 1401
- Barnes, J., & Kasen, D. 2013, *ApJ*, 775, 18
- Bartos, I., Brady, P., & Márka, S. 2013, *Classical and Quantum Gravity*, 30, 123001
- Bartos, I., Crotts, A. P. S., & Márka, S. 2015, *ApJ*, 801, L1
- Becker, A. 2015, HOTPANTS: High Order Transform of PSF AND Template Subtraction, Astrophysics Source Code Library, ascl:1504.004
- Belczynski, K., Kalogera, V., & Bulik, T. 2002, *ApJ*, 572, 407
- Berry, C. P. L., Mandel, I., Middleton, H., et al. 2015, *ApJ*, 804, 114
- Bertin, E., & Arnouts, S. 1996, *A&AS*, 117, 393



- Bertin, E., Mellier, Y., Radovich, M., et al. 2002, in *Astronomical Society of the Pacific Conference Series*, Vol. 281, *Astronomical Data Analysis Software and Systems XI*, ed. D. A. Bohlender, D. Durand, & T. H. Handley, 228
- Bilicki, M., Jarrett, T. H., Peacock, J. A., Cluver, M. E., & Steward, L. 2014, *ApJS*, 210, 9
- Bloom, J. S., Holz, D. E., Hughes, S. A., et al. 2009a, *ArXiv e-prints*, arXiv:0902.1527
- Bloom, J. S., Perley, D. A., Li, W., et al. 2009b, *ApJ*, 691, 723
- Branchesi, M. 2016, in *Journal of Physics Conference Series*, Vol. 718, *Journal of Physics Conference Series*, 022004
- Burrows, D. N., Grupe, D., Capalbi, M., et al. 2006, *ApJ*, 653, 468
- Butler, N., Gehrels, N., Golkhou, V. Z., et al. 2015, *Gamma Ray Coordinates Network Circular*, 18455
- Butler, N., Klein, C., Fox, O., et al. 2012, in *Proc. SPIE*, Vol. 8446, *Ground-based and Airborne Instrumentation for Astronomy IV*, 844610
- Chen, H.-Y., & Holz, D. E. 2013, *Physical Review Letters*, 111, 181101
- Connaughton, V., Burns, E., Goldstein, A., et al. 2016, *ApJ*, 826, L6
- Cutler, C., & Flanagan, É. E. 1994, *Phys. Rev. D*, 49, 2658
- Dalya, G., Frei, Z., Galgoczi, G., Raffai, P., & de Souza, R. S. 2016, *VizieR Online Data Catalog*, 7275
- Díaz, M. C., Beroiz, M., Peñuela, T., et al. 2016, *ApJ*, 828, L16
- Evans, P. A., Kennea, J. A., Barthelmy, S. D., et al. 2016, *MNRAS*, 460, L40
- Fong, W., Berger, E., Chornock, R., et al. 2013, *ApJ*, 769, 56
- Gehrels, N., Cannizzo, J. K., Kanner, J., et al. 2016, *ApJ*, 820, 136
- Golkhou, V. Z., Butler, N., Gehrels, N., et al. 2015a, *Gamma Ray Coordinates Network Circular*, 18500
- . 2015b, *Gamma Ray Coordinates Network Circular*, 20485
- Golkhou, V. Z., & Butler, N. R. 2014, *ApJ*, 787, 90
- Golkhou, V. Z., Butler, N. R., & Littlejohns, O. M. 2015c, *ApJ*, 811, 93
- Hanna, C., Mandel, I., & Voudsen, W. 2014, *ApJ*, 784, 8
- Jin, Z.-P., Li, X., Cano, Z., et al. 2015, *ApJ*, 811, L22
- Jin, Z.-P., Hotokezaka, K., Li, X., et al. 2016, *Nature Communications*, 7, 12898
- Kasliwal, M. M., Cenko, S. B., Singer, L. P., et al. 2016, *ApJ*, 824, L24
- Kessler, R., Marriner, J., Childress, M., et al. 2015, *AJ*, 150, 172
- Kouveliotou, C., Meegan, C. A., Fishman, G. J., et al. 1993, *ApJ*, 413, L101
- Lee, W. H., & Ramirez-Ruiz, E. 2007, *New Journal of Physics*, 9, 17
- LIGO Scientific Collaboration. 2015, *Gamma Ray Coordinates Network Circular*, 18626
- Littlejohns, O. M., Butler, N. R., Cucchiara, A., et al. 2014, *AJ*, 148, 2
- Metzger, B. D. 2017, *Living Reviews in Relativity*, 20, 3
- Metzger, B. D., & Berger, E. 2012, *ApJ*, 746, 48
- Nakar, E. 2007, *Phys. Rep.*, 442, 166
- Nissanke, S., Holz, D. E., Hughes, S. A., Dalal, N., & Sievers, J. L. 2010, *ApJ*, 725, 496
- Nissanke, S., Kasliwal, M., & Georgieva, A. 2013, *ApJ*, 767, 124
- Phinney, E. S. 1991, *ApJ*, 380, L17
- Piran, T. 1999, *Phys. Rep.*, 314, 575
- Piran, T., Nakar, E., & Rosswog, S. 2013, *MNRAS*, 430, 2121
- Rabinowitz, D., Baltay, C., Ellman, N., Woodward, E., & Nugent, P. 2015, *Gamma Ray Coordinates Network Circular*, 18473
- Rees, M. J., & Meszaros, P. 1992, *MNRAS*, 258, 41P
- Rezzolla, L., Giacomazzo, B., Baiotti, L., et al. 2011, *ApJ*, 732, L6
- Roberts, L. F., Kasen, D., Lee, W. H., & Ramirez-Ruiz, E. 2011, *ApJ*, 736, L21
- Rosswog, S., Korobkin, O., Arcones, A., Thielemann, F.-K., & Piran, T. 2014, *MNRAS*, 439, 744
- Ruiz, M., Lang, R. N., Paschalidis, V., & Shapiro, S. L. 2016, *ApJ*, 824, L6
- Singer, L., Shawhan, P., Palliyaguru, N., et al. 2015a, *Gamma Ray Coordinates Network Circular*, 18442
- Singer, L. P., Kasliwal, M. M., Ferretti, R., et al. 2015b, *Gamma Ray Coordinates Network Circular*, 18497
- Singer, L. P., Chen, H.-Y., Holz, D. E., et al. 2016, *ApJ*, 829, L15
- Smartt, S. J., Chambers, K. C., Smith, K. W., et al. 2016, *MNRAS*, 462, 4094
- Soares-Santos, M., Kessler, R., Berger, E., et al. 2016, *ApJ*, 823, L33
- Szalay, A. S., Connolly, A. J., & Szokoly, G. P. 1999, *AJ*, 117, 68
- Tanvir, N. R., Levan, A. J., Fruchter, A. S., et al. 2013, *Nature*, 500, 547
- Thorne, K. S. 1987, *Gravitational radiation.*, ed. S. W. Hawking & W. Israel, 330–458
- Troja, E., Read, A. M., Tiengo, A., & Salvaterra, R. 2016a, *ApJ*, 822, L8
- Troja, E., Sakamoto, T., Cenko, S. B., et al. 2016b, *ApJ*, 827, 102
- Watson, A. M., Richer, M. G., Bloom, J. S., et al. 2012, in *Proc. SPIE*, Vol. 8444, *Ground-based and Airborne Telescopes IV*, 84445L
- White, D. J., Daw, E. J., & Dhillon, V. S. 2011, *Classical and Quantum Gravity*, 28, 085016

TABLE 1  
OBSERVATIONS LOG

#	RA (J2000)	DEC (J2000)	20151023 total exp. (sec)		20151024 total exp. (sec)		20151025 total exp. (sec)	
			<i>r</i> -band	<i>i</i> -band	<i>r</i> -band	<i>i</i> -band	<i>r</i> -band	<i>i</i> -band
1	0.493792	-15.461389	480.0	480.0	560.0	560.0	720.0	720.0
2	2.485667	-24.963111	480.0	480.0	480.0	480.0	640.0	720.0
3	3.516292	-23.182111	240.0	240.0	320.0	400.0	720.0	640.0
4	3.855459	-21.444805	480.0	480.0	240.0	240.0	480.0	400.0
5	4.797917	-22.668389	480.0	480.0	240.0	320.0	480.0	480.0
6	8.70375	7.450389	720.0	720.0	960.0	960.0	–	–
7	10.765958	-22.246806	240.0	240.0	480.0	480.0	640.0	640.0
8	11.785666	-20.760389	480.0	480.0	400.0	240.0	720.0	560.0
9	11.888083	-25.288805	240.0	240.0	240.0	240.0	480.0	480.0
10	12.338083	-18.075889	480.0	480.0	240.0	400.0	720.0	720.0
11	12.457792	-21.012194	720.0	720.0	480.0	480.0	800.0	800.0
12	12.60225	-19.906194	720.0	720.0	480.0	480.0	960.0	960.0
13	12.800083	12.024611	1200.0	1200.0	880.0	800.0	1200.0	880.0
14	16.225667	2.133305	1200.0	1200.0	960.0	960.0	1200.0	1200.0
15	16.943708	1.0635	1200.0	1200.0	960.0	960.0	1200.0	1120.0
16	20.3295	12.411694	1440.0	1440.0	880.0	880.0	1200.0	1200.0
17	22.828792	7.787694	1440.0	1440.0	960.0	960.0	1200.0	1200.0
18	352.150792	14.743	480.0	480.0	480.0	480.0	720.0	720.0
19	7.464167	-16.165111	480.0	480.0	480.0	480.0	640.0	640.0
20	6.54525	-11.053889	480.0	480.0	640.0	640.0	–	–
21	5.965667	-24.705111	480.0	480.0	400.0	400.0	480.0	480.0
22	2.30025	-26.161111	240.0	240.0	320.0	320.0	480.0	400.0
23	5.173792	8.615389	720.0	720.0	960.0	720.0	–	–
24	13.197917	-26.59	480.0	480.0	320.0	320.0	560.0	560.0
25	346.6845	12.771889	480.0	480.0	480.0	480.0	720.0	720.0
26	347.1105	-15.611389	240.0	240.0	–	–	480.0	480.0